

冷喷涂-激光熔覆车轴组织及性能研究

吕培源, 余敏*, 罗斌, 陈琴, 陈辉

西南交通大学材料科学与工程学院四川省先进焊接及表面工程中心, 四川 成都 610031

摘要 采用冷喷涂-激光熔覆顺序耦合技术,在高速列车车轴钢 EA4T 表面制备 Ni30 冷喷涂中间层后,采用激光熔覆技术制备 Fe314 涂层,以研究冷喷层作为激光熔覆中间层对激光熔覆车轴组织及性能的影响。试验结果表明, Ni30 涂层对熔覆层和热影响区组织形貌没有影响,但改变了熔覆层界面处元素含量,并减小了热影响区面积。激光热导致强烈塑性变形的 Ni30 颗粒界面发生熔化,涂层与车轴钢由机械结合变为冶金结合,剪切强度由 35.9 MPa 提高为 224.4 MPa。在性能方面, Ni30 中间层导致复合试样熔覆层、热影响区的硬度和剪切强度均降低,塑韧性得到提升,从而性能更接近基体。但过多的激光热导致冷喷涂 Ni30 气孔聚集长大,且受激光热作用后涂层结合强度比单熔覆试样低 115 MPa 左右,因而接下来仍需对工艺进行优化。

关键词 激光技术; 激光熔覆; 冷喷涂; 热影响区; 组织与性能

中图分类号 TG178 **文献标志码** A

DOI: 10.3788/CJL221272

1 引言

车轴是高速列车最重要的零部件之一。在列车运行过程中,车轴在各种交变载荷下,极易发生疲劳破坏。据统计,疲劳裂纹造成的车轴失效数量占 90% 以上^[1]。因疲劳裂纹通常在表面萌生,所以提高列车车轴表面性能显得至关重要^[2]。

激光熔覆技术具有稀释率低、冶金结合强度高^[3-4]以及熔覆层厚可控等优势^[5-7],已被用于车轴表面涂层制备和修复。澳大利亚墨尔本“硬铬工程”有限公司最先采用激光熔覆技术修复车轴,该公司认为激光熔覆技术热输入量小的特点可以有效地减少再制造过程中车轴的热损伤,且再制造一根车轴的成本仅为更换新车轴的 40%^[8]。随后皇家墨尔本理工大学尝试采用 420 不锈钢和 CrMoV 合金对车轴进行修复。结果表明,420 不锈钢再制造车轴疲劳寿命比原始车轴低 8.4%,而 CrMoV 再制造试样比原始车轴高 16.9%^[9]。因此从国外的报道可以看出,当前激光再制造车轴的疲劳寿命还达不到原轴的寿命。

在国内,李丛辰等^[10]采用激光熔覆技术在 EA4T 车轴钢表面制备了 Fe314 合金修复层,相较于基体试样,再制造试样的抗拉强度提高,但屈服强度降低,韧性和塑性降低。Chen 等^[11]进一步表征了该试样的疲劳性能,发现带熔覆层的试样在相同的应力强度因子范围下具有较低的裂纹扩展速率,因此认为激光熔覆提高了 EA4T 车轴钢在低载荷条件下的疲劳寿命。为

了进一步改善熔覆层塑韧性,陈林等^[12]通过施加超声振动熔池,打碎了熔覆层枝晶以减少枝晶偏析,从而细化了晶粒,显著提高了熔覆层硬度。陈文静等^[13]通过向自主设计的 FeCrNiMo 合金粉末中加入稀土元素 La 和 Ce 细化了熔覆层的晶粒,提高了再制造试样的抗拉强度和屈服强度。可见,国内陈文静团队主要通过调整工艺和熔覆材料成分来改善熔覆层的塑韧性,以期提升再制造车轴的疲劳寿命。

侯有忠等^[14]通过比较车轴钢熔覆 Fe310、Fe314、Fe316 以及 NiCrMo 涂层性能,发现 NiCrMo 合金熔覆层具有最佳的力学性能,并指出需要寻找进一步的解决方案来应对激光熔覆对基体的热输入问题以及熔覆层存在非稳态组织的问题。激光熔覆过程中钢基体材料的热量输入会导致热影响区(HAZ)发生马氏体转变^[15-16]。马氏体组织具有低的塑性和断裂韧性,多年来被各国铁路标准协会禁止^[17-19]。钢轨激光熔覆研究现状指出:HAZ 的组织及性能是影响激光熔覆钢轨疲劳性能的关键因素。Lewis 等^[20]研究了钢轨激光熔覆 Stellite 6 熔覆层的四点弯曲疲劳断口,结果表明,裂纹起裂于熔覆层中的夹杂和熔覆层与 HAZ 区的界面,并向基体扩展。研究者推论,HAZ 区的脆性特征不足以抵抗此区所承受的高应力,从而使整体结构疲劳性能降低。方金祥等^[21]在对 Incone718 合金进行激光熔覆试验时,提出减少热影响区的宽度有助于零件质量的改善。因此如何减少并消除热影响区中的马氏体组织脆硬特征成为

收稿日期: 2022-09-26; 修回日期: 2022-10-26; 录用日期: 2022-11-15; 网络首发日期: 2022-11-21

基金项目: 四川省青年科学基金项目(2022NSFSC1933)

通信作者: *yumin@home.swjtu.edu.cn

了研究中关注的热点之一。

冷喷涂技术是 20 世纪 80 年代被提出的一种新材料表面改性技术。冷喷涂技术主要通过粒子高速撞击形成涂层,因而相比于传统热喷涂方法,可有效避免热作用引起的高温氧化、相变、晶粒长大等问题^[22-23]。冷喷涂技术具有沉积温度低、喷涂效率高、涂层致密度高且对基体无热影响等优点,已被广泛用于各类零部件表面修复^[24-25]。例如,Widener 等^[26]使用高压冷喷涂在 6061Al 液压阀体上修复了阀门执行器的内孔密封表面,使零件恢复使用。美国军方研究实验室使用便携式高压冷喷设备在直升飞机的 ZE41A 镁合金表面喷涂 CP-Al 材料,修复了腐蚀损伤^[27]。

本文从激光再制造钢轨中 HAZ 大小和组织对疲

劳性能的显著影响入手,基于冷喷涂对基体无热影响且冷喷涂中间层对输入基体激光热的吸收作用,采用冷喷涂-激光熔覆顺序耦合技术,构建了新型车轴表面功能涂层。研究了冷喷涂层作为激光熔覆中间层对激光熔覆热影响区的影响,并对所制备涂层的组织、力学性能进行了观察与分析。

2 试验材料及方法

2.1 试验材料

基体材料选用退火态车轴钢 EA4T 钢,化学成分如表 1 所示。EA4T 钢组织由片层状珠光体和白色铁素体组成,如图 1 所示,其中 OM 为光学显微镜,SEM 为扫描电镜。

表 1 EA4T 车轴钢的化学成分(质量分数,%)
Table 1 Chemical compositions of EA4T (mass fraction, %)

C	Si	Mn	P	S	Cr	Cu	Mo	Ni	Fe
0.200-0.290	0.150-0.400	0.500-0.800	0.020	0.015	0.900-1.200	0.300	0.150-0.300	0.300	Bal.

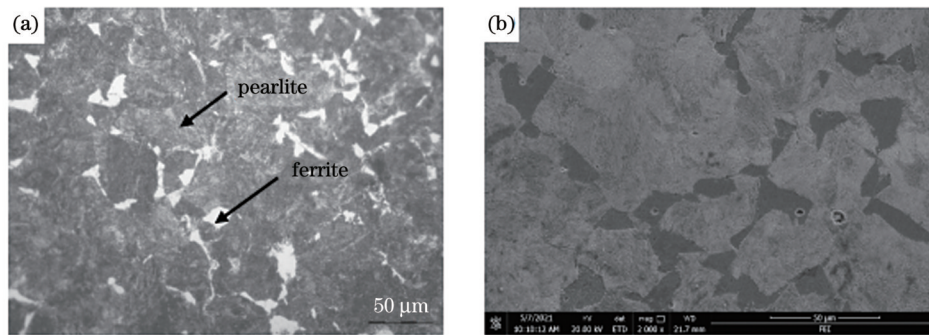


图 1 EA4T 显微组织。(a)光学显微镜;(b)扫描电镜
Fig. 1 Microstructures of EA4T. (a) OM; (b) SEM

激光熔覆粉末选用 Fe314 (Fe-17.5Cr-10.5Ni-0.65B-0.12Si-0.1C)。冷喷涂粉末选用 Ni30(Ni 质量分

数为 30%,Fe 质量分数为 70%),由铁基粉末与镍基粉末机械混合而成,粒径为 10~60 μm。粉末形貌如图 2 所示。

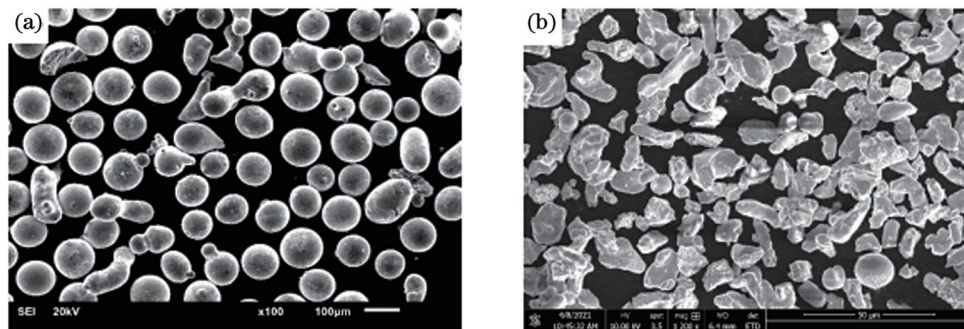


图 2 SEM 形貌。(a) Fe314;(b) Ni30
Fig. 2 SEM morphologies. (a) Fe314; (b) Ni30

2.2 试验设备及工艺

激光熔覆技术采用 Nd:YAG 激光器,冷喷涂设备为冷喷涂系统,如图 3 所示。激光熔覆工艺参考课题组前期优化参数,而冷喷涂参数以金相观察涂层与基体界面结合良好为准,两种方法优化后的工艺

参数如表 2 所示。首先,在 EA4T 车轴钢基体上制备冷喷涂 Ni30 涂层,厚度约为 1 mm,用砂纸打磨去除氧化膜后,熔覆 Fe314 制备复合涂层试样。同时采用相同的工艺参数制备单激光熔覆 Fe314 涂层作为比较。

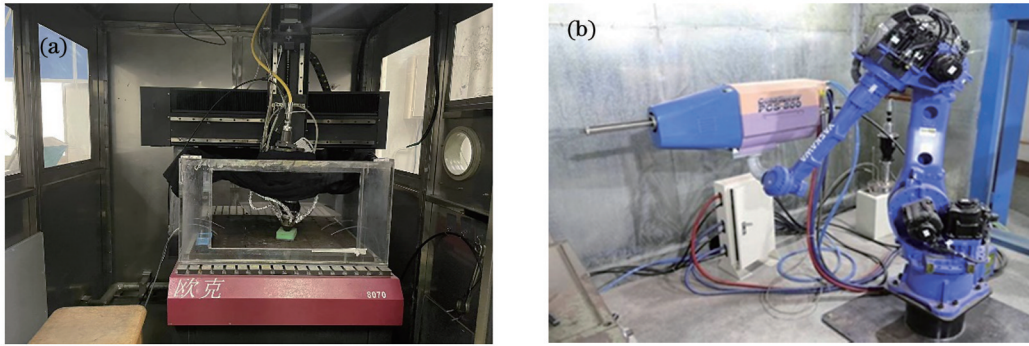


图 3 试验设备。(a)激光熔覆;(b)冷喷涂

Fig. 3 Experimental equipments. (a) Laser cladding; (b) cold spraying

表 2 冷喷涂-激光熔覆工艺参数

Table 2 Cold spraying and laser cladding process parameters

Cold spraying		Laser cladding	
Parameter	Content	Parameter	Content
Propellant gas	N ₂	Flow rate of protect gas N ₂ /(L/min)	30
Gas pressure /MPa	5	Laser power /W	2400
Temperature /°C	900	Scan speed /(mm/s)	5
Powder feeder speed /(r/min)	8	Powder feed rate /(g/min)	23
Gun speed /(mm/s)	500	Spot diameter /mm	4

2.3 表征方法

使用体式显微镜观察样品的外观形貌。使用光学显微镜和扫描电子显微镜对涂层、热影响区组织及微断裂口形貌进行观察。采用扫描电子显微镜搭配的能谱仪(EDS)研究样品的化学元素分布与含量。使用Image-Pro Plus 6.0软件统计冷喷涂层孔隙率。使用数显显微硬度计对涂层的显微维氏硬度进行测试,载荷为200 g,保载时间为15 s。在万能力学试验机上进行微型剪切试验,剪切速度为3 mm/min,剪切试验示意图如图4所示。

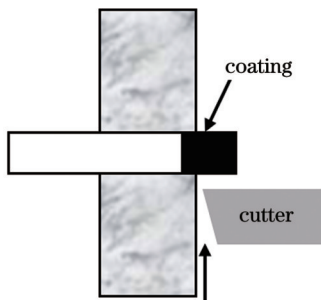


图 4 剪切试验示意图

Fig. 4 Schematic of shear test

3 试验结果及讨论

3.1 冷喷涂 Ni30 涂层

图5(a)为冷喷涂 Ni30 涂层形貌及元素分布图。Ni30 颗粒经氮气加速撞击基材材料后发生强烈塑性变形,呈扁平状,变形颗粒不断堆垛形成片层状涂层结

构并伴有孔隙,涂层孔隙率约为3.17%。从EDS结果可以看出,Ni颗粒不均匀分布于Fe变形颗粒间,涂层以变形Fe颗粒为主。这是因为,冷喷涂所用Ni30粉末为Ni基粉末和Fe基粉末的机械混合,机械混合是导致冷喷涂Ni元素分布不均匀的原因。图5(b)为冷喷涂Ni30涂层与基体界面的SEM形貌图,涂层颗粒以机械咬合方式与基体结合良好。

冷喷涂Ni30涂层硬度如图6所示。在横向测试中,涂层横截面中线位置的硬度均值为(229.89±11.80)HV,基体硬度为(234.63±7.60)HV,涂层与基体硬度相差不大。在纵向测试中,在涂层上表面沿基体方向进行硬度打点,测量三个道次。涂层硬度值波动较基体更大,这与冷喷涂涂层的组织均匀性相关(图5):一方面涂层下部因上部涂层的夯实作用更为致密,硬度值高;另一方面,涂层中孔隙和颗粒界面处硬度值低;最后,本文中喷涂的Ni30为机械混合粉末,且Ni颗粒的不均匀分布也可能导致硬度值的波动。

3.2 激光熔覆组织

图7为复合涂层及单熔覆涂层组织。复合涂层组织[图7(a)]上部为激光熔覆层,下部为冷喷涂层,二者之间有一条明显的亮白带,是冶金结合的标志。复合涂层与单熔覆涂层激光区域组织一致:在熔覆层底部,由界面向上,晶粒形态依次由平面晶过渡到柱状晶,再到树枝晶。在熔池凝固时,晶粒生长的方式主要受温度梯度G与凝固速度R的影响。在熔池底部,由于熔池靠近基材/Ni30涂层,此处温度梯度G最大,而由于固液界面处液相过冷度小,凝固速度R最小,因此

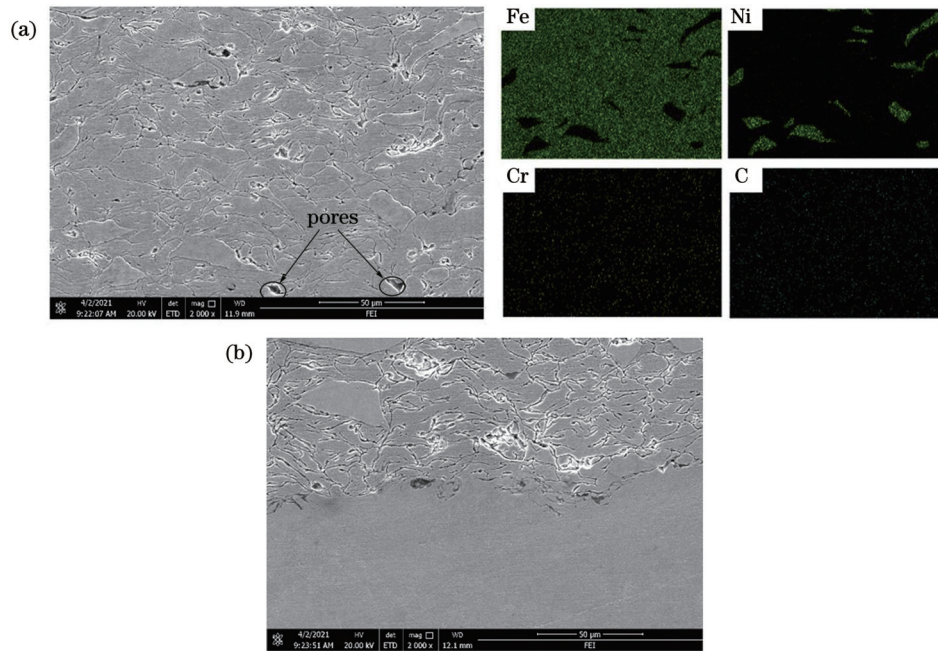


图 5 冷喷涂 Ni30 涂层的 SEM 图。(a) 截面；(b) 界面

Fig. 5 SEM images of cold sprayed Ni30 coating. (a) Cross section; (b) interface

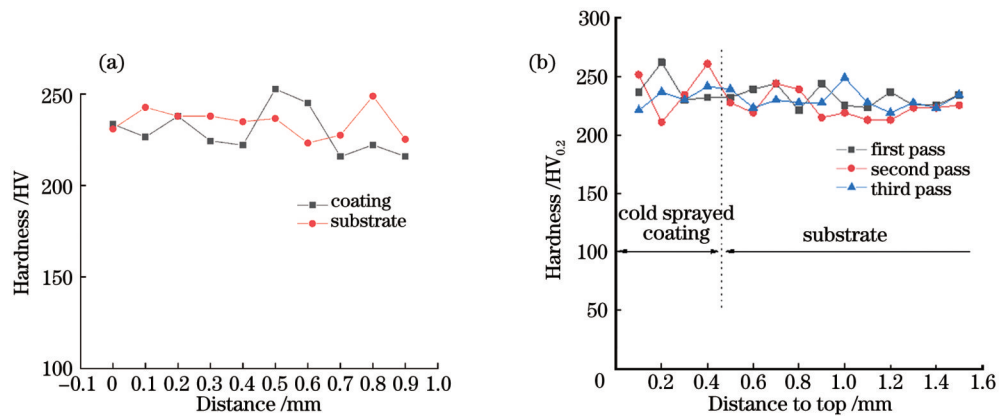


图 6 冷喷涂 Ni30 涂层硬度曲线。(a) 横向；(b) 纵向

Fig. 6 Hardness curves of cold sprayed Ni30 coating. (a) Transverse; (b) longitudinal

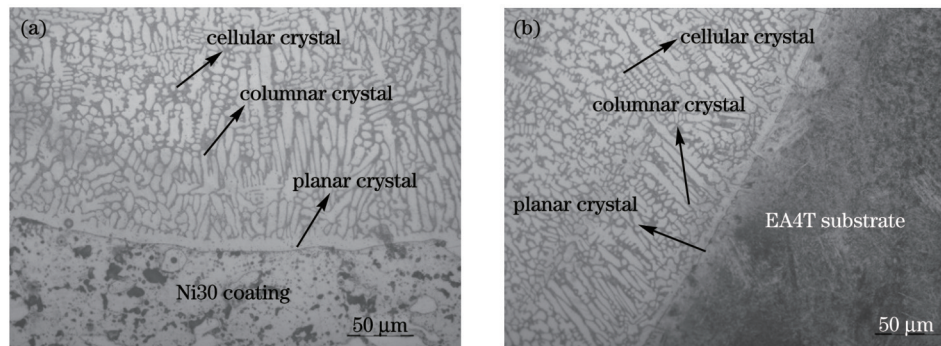


图 7 激光熔覆涂层组织。(a) 复合涂层；(b) 单熔覆涂层

Fig. 7 Microstructures of laser cladding coating. (a) Composite coating; (b) single cladding coating

靠近此区域内晶粒的生长方式为平面状。随着与熔池底部距离的增加, G 逐渐减小而 R 逐渐增大, 所以晶粒生长方式逐渐转变为胞状树枝状, 如图 8 所示。结合 SEM 和电子背散射衍射 (EBSD) 结果可见, 从组织而言, 冷喷涂 Ni30 中间层对激光熔覆层组织没有影响,

两者熔覆层中枝晶组织为 γ 相, 枝晶间主要为 δ 相与 $M_{23}C_6$ 型碳化物形成的共晶组织, $M_{23}C_6$ 型碳化物主要分布在 γ/δ 相界位置。张杰等^[28] 在 IN718 激光熔覆层组织中也发现了 $M_{23}C_6$ 型碳化物。对熔覆层底部不同元素分布进行面扫描, 分析了 Fe、Cr、Ni 以及 C 四种化

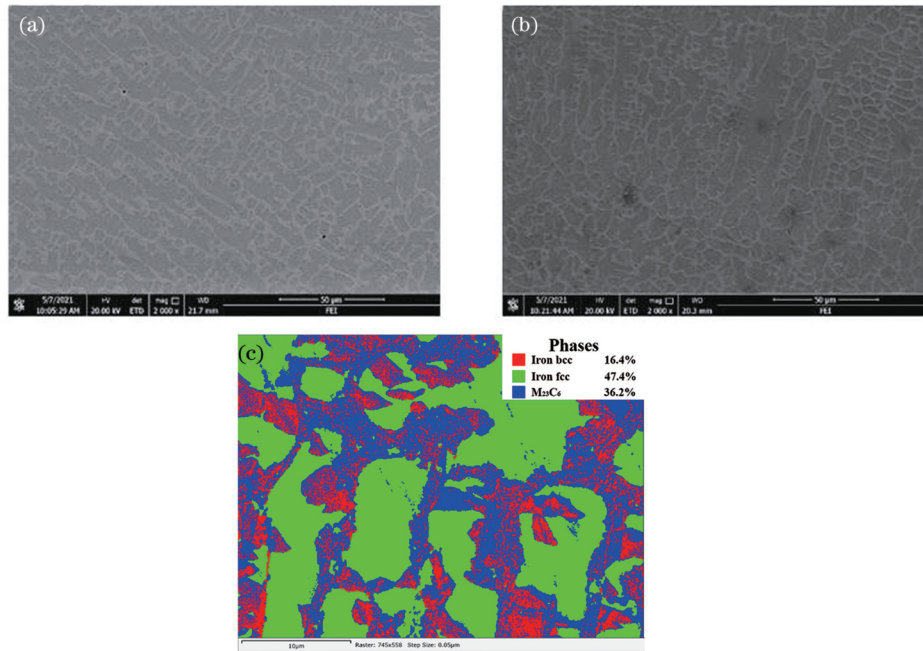


图 8 熔覆层 SEM 形貌及物相分布 EBSD 照片。(a)复合涂层;(b)单熔覆涂层;(c)熔覆层物相分布 EBSD 照片
Fig. 8 SEM micrographs and phase distribution EBSD photo of cladding layer. (a) Composite coating; (b) single cladding coating; (c) phase distribution EBSD photo of cladding layer

学元素的分布(图9)及含量(表3),冷喷涂 Ni30 涂层对激光熔覆 Fe314 层有稀释作用,Fe 含量减少,Ni 含量增加。冷喷涂所采用的 Ni30 粉末由质量分数为 30% 的 Ni 和质量分数为 70% 的 Fe 组成,激光熔覆粉末 Fe314 中的 Fe、Ni 含量(质量分数)分别为~72% 和 10.5%,与

基材 EA4T 中的 Fe(~97% 质量分数)、Ni(0.3% 质量分数)元素有较大差异,当界面发生互扩散时,各元素的浓度差异及交互影响导致界面处合金元素含量不同。潘浒等^[29]的试验证实,在一定参数范围内,稀释率受激光功率影响,并呈正相关关系。

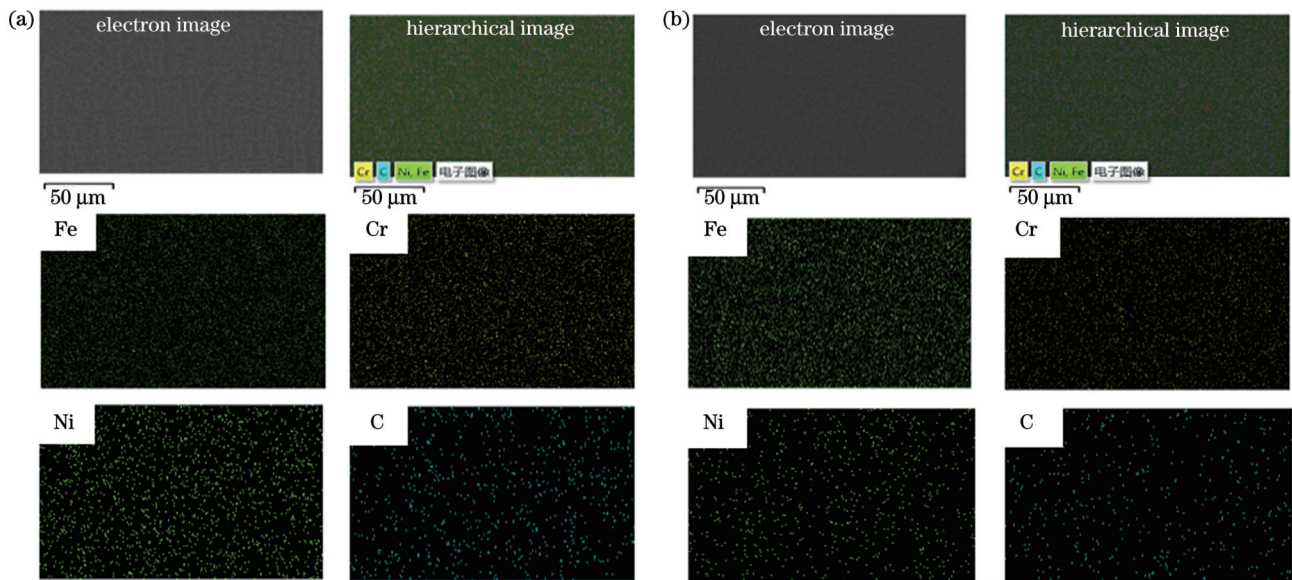


图 9 熔覆层底部化学元素的 EDS 图。(a)复合涂层;(b)单熔覆涂层
Fig. 9 EDS images of chemical elements at bottom of cladding layer. (a) Composite coating; (b) single cladding coating

表 3 底部化学元素的 EDS 检测结果(质量分数,%)
Table 3 EDS detection results of bottom chemical elements (mass fraction, %)

Sample	Fe	Ni	Cr	C	Si
Laser cladding sample	73.36	6.12	12.08	7.61	0.18
Composite sample	65.66	9.94	13.52	10.21	0.66

3.3 热影响区组织

图 10 为复合和单熔覆单道试样热影响区形状照片。因冷喷涂 Ni30 涂层对输入到基材的激光热量的吸收,冷喷涂-激光熔覆复合涂层的热影响区呈扇形。中间层的阻隔作用导致激光能量在被中间层吸收后传入基体,距离激光束最近的热影响区最深。单激光熔覆试样的热影响区呈半圆环型,热量从熔池底部向基体以热传导的方式传递,此时熔池内部温度基本一致,热影响区温度梯度一致,因而其热影响区是以激光束在基材表面的焦点为圆心的半圆环型。在体视显微镜下对热影响区深度进行测量,得到复合涂层热影响区最大深度约为 0.86 mm,单熔覆为 4.17 mm。使用 Image-pro plus 对两组试样的热影响区面积进行计算,以冷喷涂层为中间层的复合试样的热影响区平均面积为 1542750 pixel²,与单熔覆试样的热影响区的 1749265 pixel²平均面积相比,减少了 13.39%。

图 11 为复合和单熔覆试样热影响区组织。激光

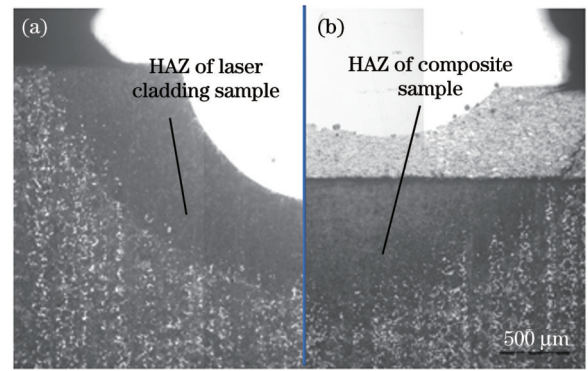


图 10 热影响区形状。(a)激光熔覆试样;(b)复合试样
Fig. 10 Shapes of heat affected zones. (a) Laser cladding sample; (b) composite sample

熔覆过程中,热影响区被加热到临界温度以上,发生奥氏体化,随后激光束移开,该位置在快速冷却过程中发生马氏体相变,因此两个试样均在热影响区生成了细小板条状马氏体组织[图 11(a)~(d)]。冷喷涂 Ni30

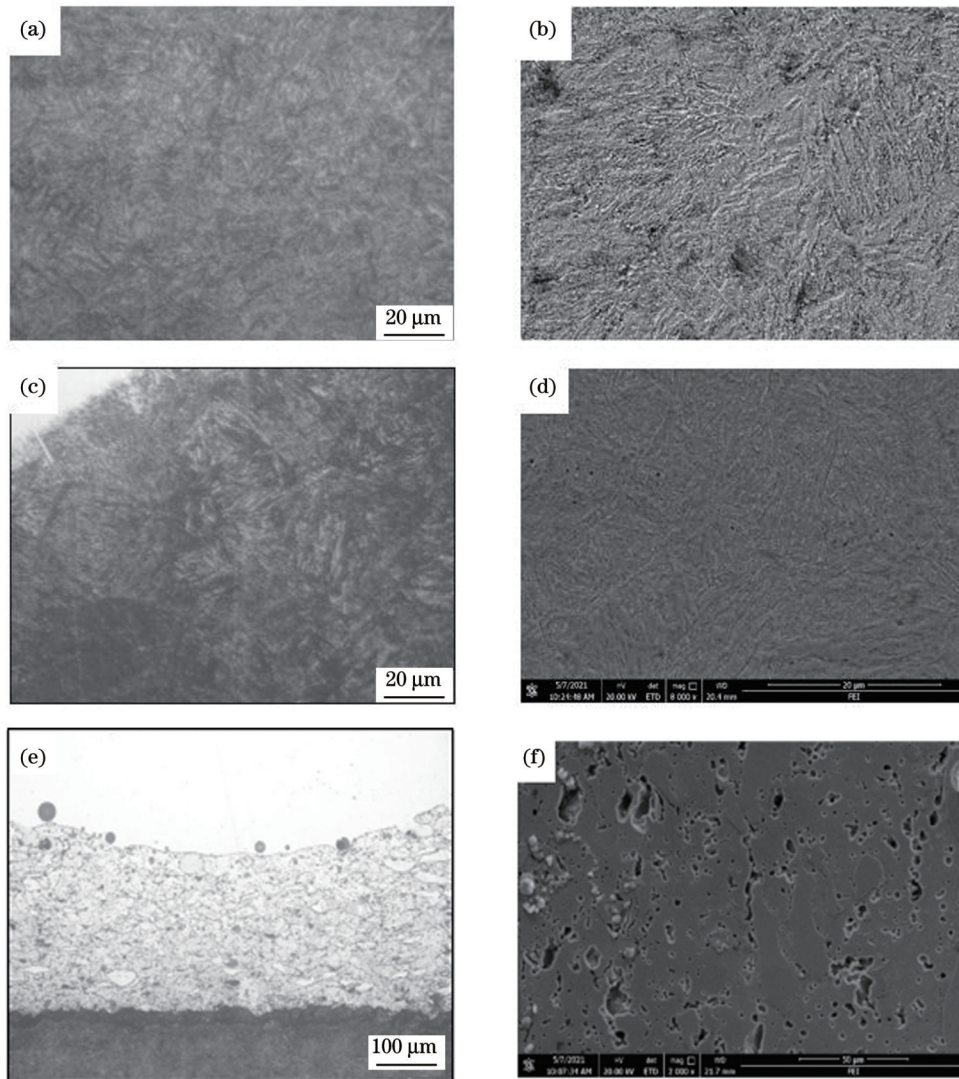


图 11 激光熔覆热影响区组织。(a)复合涂层;(b)单熔覆涂层;(c)冷喷涂 Ni30 中间层;(d)~(f)图 11(a)~(c)对应的 SEM 图
Fig. 11 Microstructures of laser cladding heat affected zones. (a) Composite coating; (b) single cladding coating; (c) cold sprayed Ni30 middle layer; (d)~(f) SEM images corresponding to Figs. 11(a)~(c)

中间层受激光热作用,原强烈塑性变形颗粒(图 5)受热发生回复,且界面发生溶解,形成类似铸态组织,气孔聚集长大。冷喷涂涂层吸收过多热量后发生克肯达尔效应,气孔聚集长大,因此研究后期将考虑进一步调整激光熔覆工艺。

3.4 显微硬度

图 12 为复合试样和单熔覆试样的显微硬度曲线,其中 C-S layer 表示冷喷涂层。根据熔覆层中上部、熔覆层稀释区、热影响区和基材区,将硬度值曲线分为四段。

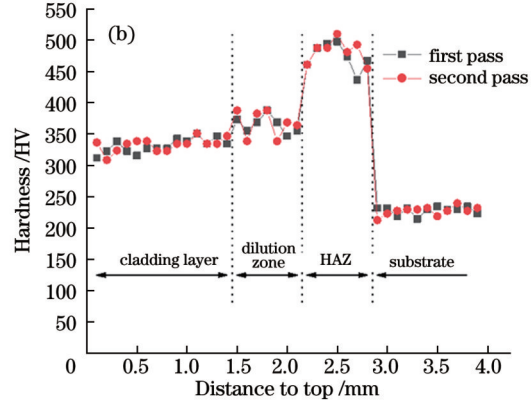
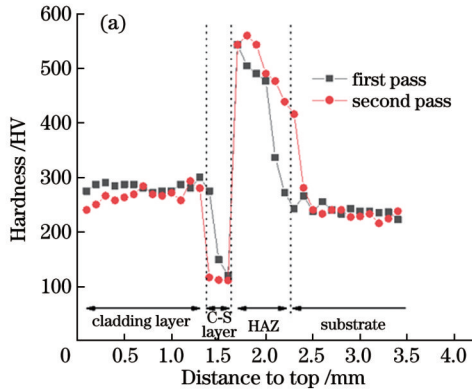


图 12 显微硬度曲线。(a)复合涂层;(b)单激光熔覆

Fig. 12 Microhardness curves. (a) Composite coating; (b) single laser cladding

3.5 剪切性能

图 13 为复合试样及单熔覆试样各区的剪切强度及截面切入率对比。首先,对于熔覆层,复合涂层与单熔覆涂层组织相同(图 8),复合熔覆层剪切强度比单熔覆层略低 25 MPa,截面切入率增加 53%;对于热影响区, Ni30 中间层不仅改变了热影响区面积,削弱了激光热对基体的影响,导致复合涂层热影响区强度差异,复合涂层更少的热输入导致热影响区强度比单熔覆热影响区低 233.2 MPa,更接近于基体的剪切强度,塑韧性增加;对于涂层与基体界面的剪切强度,喷涂态 Ni30 与 EA4T 的初始结合为机械结合,平均剪

复合试样熔覆层平均硬度为 275.1 HV, 低于单熔覆的硬度值 331.8 HV, 这是因为两个试样在此区域的合金元素不同(表 3)。受激光热影响后的 Ni30 涂层硬度为 121.8 HV, 低于喷涂态硬度 229.9 HV, 这是喷涂态的冷作硬化受激光热影响后消失及气孔的长大作用所导致[图 11(f)]。复合试样热影响区硬度为 458.2 HV, 略低于单熔覆试样 478.3 HV, 这是因为中间层的加入使激光的透过率降低,一部分能量被其吸收,使基体的加热温度降低,冷却速度变缓,马氏体转变程度降低。

切强度为 35.9 MPa, 受激光热作用后发生冶金结合, 结合强度增加为 224.4 MPa, 低于单熔覆界面强度(339.6 MPa)。为进一步探究中间层对熔覆层及热影响剪切性能的影响,对复合试样以及单熔覆试样的熔覆层和热影响区的断口形貌进行观察,如图 14 所示。复合试样熔覆层的断面略有起伏,断口上有稀疏的韧窝以及密集的撕裂棱,属于过渡断裂形式中的准解理断裂。在热影响区的断口处可以观察到剪切刀具造成的划痕,以及剪切应力造成的平坦面和一些被拉长的韧窝。单激光熔覆试样的熔覆层断口平齐,在其断口处观察到了撕裂棱的特征,属于准解理断裂。热影

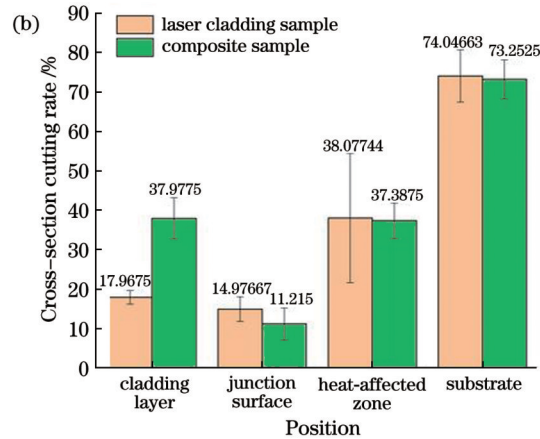
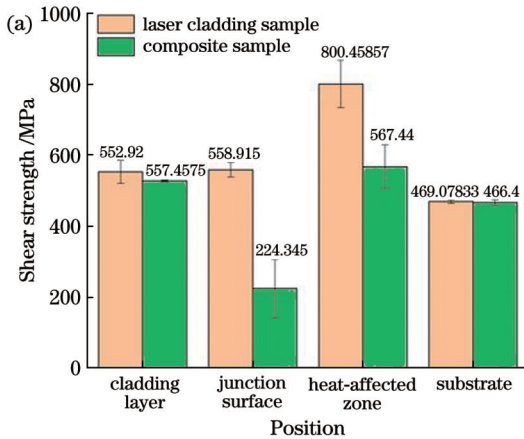


图 13 复合试样与单熔覆试样剪切性能对比。(a)剪切强度;(b)截面切入率

Fig. 13 Comparison of shear properties between composite sample and laser cladding sample. (a) Shear strength; (b) cross-section cutting rate

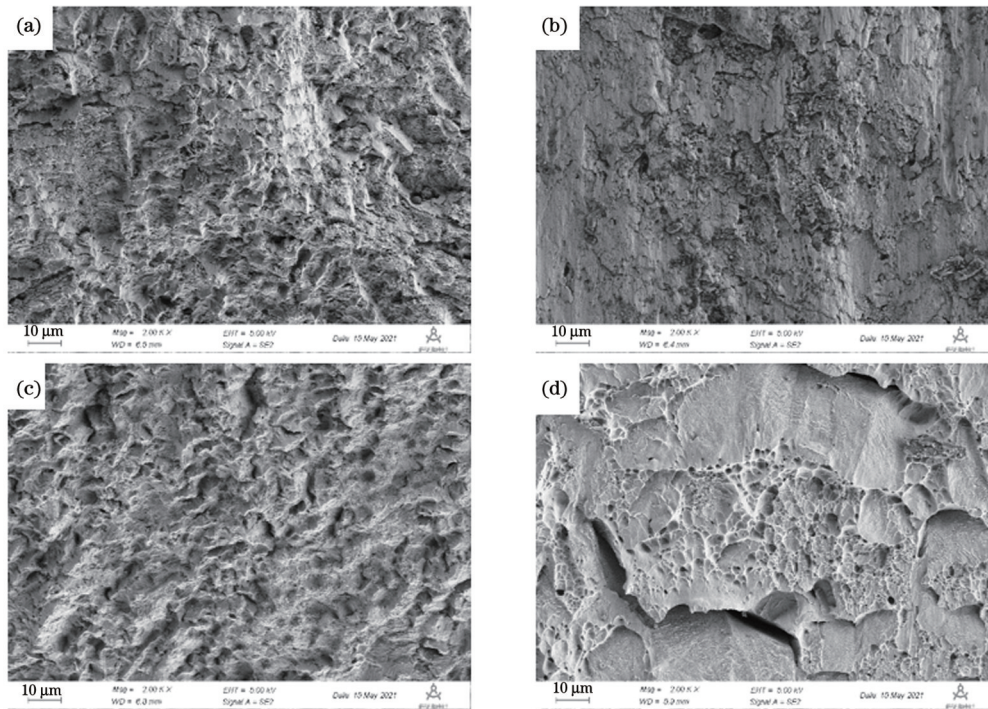


图 14 激光熔覆断口形貌。(a)复合试样熔覆层;(b)复合试样热影响区;(c)单熔覆试样熔覆层;(d)单熔覆试样热影响区
Fig. 14 Laser cladding fracture morphologies. (a) Cladding layer of composite sample; (b) HAZ of composite sample; (c) cladding layer of single cladding sample; (d) HAZ of single cladding sample

响区的断口表面有大块的平坦面以及二次裂纹,有解理断裂的特征,一些部位存在着较浅的韧窝,属于由韧窝型的韧性断裂与穿晶型的解理断裂组成的混合断裂。

4 结 论

冷喷涂 Ni30 中间层对激光熔覆层及热影响区组织形态无影响,但导致热影响区面积减小了 13.39%。喷涂态 Ni30 中间层受激光热作用后界面发生溶解,气孔长大,形成类似铸态组织。

复合试样因 Ni30 中间层的 Ni 元素稀释作用,熔覆层硬度降为 275.1 HV,低于单熔覆的硬度值 (331.8 HV),且因中间层吸引了输入到基体的激光热,复合试样热影响区硬度从单熔覆试样的 478.3 HV 降低为 458.2 HV,热影响区的韧性略微提高了。

复合涂层中冷喷涂 Ni30 中间层与基体的结合强度为 224.4 MPa,低于单熔覆界面 (339.6 MPa)。复合涂层热影响区因热输入更少,热影响区强度低于单熔覆层热影响区 (233.2 MPa),接近于基体的剪切强度。

致谢 感谢广东省科学院新材料研究所现代材料表面工程技术国家工程实验室谢迎春博士在制备冷喷涂 Ni30 涂层时提供的帮助。

参 考 文 献

[1] 杜松林,汪开忠,胡芳忠. 国内外高速列车车轴技术综述及展望

[J]. 中国材料进展, 2019, 38(7): 641-650.

- Du S L, Wang K Z, Hu F Z. Overview and prospect of axle technology for high speed trains at home and abroad[J]. Materials China, 2019, 38(7): 641-650.
- [2] 齐先胜, 侯有忠, 牛富杰, 等. 高速动车组车轴的再制造可行性分析[J]. 电焊机, 2017, 47(10): 8-15.
Qi X S, Hou Y Z, Niu F J, et al. Feasibility analysis of remanufacture of high-speed train unit axles[J]. Electric Welding Machine, 2017, 47(10): 8-15.
- [3] Zou L, Zeng D F, Wang J, et al. Effect of plastic deformation and fretting wear on the fretting fatigue of scaled railway axles[J]. International Journal of Fatigue, 2020, 132: 105371.
- [4] 王志文, 庄宿国, 刘海青, 等. 激光熔覆自润滑复合涂层研究进展及发展趋势[J]. 表面技术, 2018, 47(5): 104-112.
Wang Z W, Zhuang S G, Liu H Q, et al. Research progress and development trend of self-lubricating composite coatings by laser cladding[J]. Surface Technology, 2018, 47(5): 104-112.
- [5] Haldar B, Saha P. Problems on the development of hard and low friction *in situ* coatings on Ti-6Al-4V using laser cladding[J]. Procedia Manufacturing, 2018, 20: 446-451.
- [6] Haldar B, Saha P. Identifying defects and problems in laser cladding and suggestions of some remedies for the same[J]. Materials Today: Proceedings, 2018, 5(5): 13090-13101.
- [7] Chai Q, Fang C, Qiu X L, et al. Modeling of temperature field and profile of Ni60AA formed on cylindrical 316 stainless steel by laser cladding[J]. Surface and Coatings Technology, 2021, 428: 127865.
- [8] Soodi M. Laser cladding compared with TIG welding to repair and refurbish railway axles[C]//CORE 2010 Conference on Railway Engineering, September 12-15, 2010, Wellington, New Zealand. Washington, D. C.: The National Academies of Sciences, Engineering, and Medicine, 2010.
- [9] Soodi M. Investigation of laser deposited wear resistant coatings on railway axle steels[D]. Melbourne Victoria: RMIT University, 2013.
- [10] 李丛辰, 陈文静, 向超, 等. EA4T 钢表面激光熔覆 Fe314 合金熔覆层的微观组织及性能[J]. 电焊机, 2016, 46(5): 73-77.
Li C C, Chen W J, Xiang C, et al. Microstructure and properties

- of Fe314 alloy cladding layer by laser cladding on EA4T steel[J]. Electric Welding Machine, 2016, 46(5): 73-77.
- [11] Chen W J, Chen H, Li C C, et al. Microstructure and fatigue crack growth of EA4T steel in laser cladding remanufacturing[J]. Engineering Failure Analysis, 2017, 79: 120-129.
- [12] 陈林, 陈文静, 黄强, 等. 超声振动对 EA4T 钢激光熔覆质量和性能的影响[J]. 材料工程, 2019, 47(5): 79-85.
Chen L, Chen W J, Huang Q, et al. Effect of ultrasonic vibration on quality and properties of laser cladding EA4T steel[J]. Journal of Materials Engineering, 2019, 47(5): 79-85.
- [13] 陈文静, 毛裕, 唐思成. 稀土对激光熔覆 EA4T 车轴微观组织和性能的影响[J]. 西华大学学报(自然科学版), 2020, 39(3): 35-41.
Chen W J, Mao Y, Tang S C. Effect of rare earth on microstructure and performance of laser cladding EA4T axle[J]. Journal of Xihua University (Natural Science Edition), 2020, 39(3): 35-41.
- [14] 侯有忠, 齐先胜, 邓鸿剑, 等. 动车组车轴增材再制造材料选择和性能评价[J]. 表面技术, 2020, 49(12): 162-169, 219.
Hou Y Z, Qi X S, Deng H J, et al. Material selection and mechanical property evaluation for additively remanufactured EMU axles[J]. Surface Technology, 2020, 49(12): 162-169, 219.
- [15] 余敏, 张鸿羽, 曹开, 等. 激光熔覆在高速列车上的应用研究现状[J]. 表面技术, 2020, 49(10): 12-20, 38.
Yu M, Zhang H Y, Cao K, et al. Application status of laser cladding in high-speed trains[J]. Surface Technology, 2020, 49(10): 12-20, 38.
- [16] 庞小通, 姚成武, 龚群甫, 等. 多层激光熔覆对 30CrMnSiNi2A 高强钢组织与性能的影响[J]. 中国激光, 2021, 48(6): 0602104.
Pang X T, Yao C W, Gong Q F, et al. Influence of multilayer laser cladding on the microstructure and properties of 30CrMnSiNi2 A steel substrate[J]. Chinese Journal of Lasers, 2021, 48(6): 0602104.
- [17] Vignole railway rails 46 kg/m and above. Appl-Track-Rail: EN 13647-1[EB/OL]. [2022-09-08]. <http://www.mydoc123.com/p-708158.html>.
- [18] Arema. Section 2: specification for steel rails[EB/OL]. [2022-09-08]. <https://www.doc88.com/p-784443711049.html>.
- [19] Standard C. Technical specifications for the procurement of 43-75 kg/m rails[EB/OL]. [2022-09-08]. <https://jz.docin.com/p-696394704.html?qq-pf-to=pcqq.c2c>.
- [20] Lewis S R, Lewis R, Goodwin P S, et al. Full-scale testing of laser clad railway track; Case study-Testing for wear, bend fatigue and insulated block joint lipping integrity[J]. Wear, 2017, 376/377: 1930-1937.
- [21] 方金祥, 王玉江, 董世运, 等. 激光熔覆 Inconel718 合金涂层与基体界面的组织及力学性能[J]. 中国机械工程, 2019, 30(17): 2108-2113.
Fang J X, Wang Y J, Dong S Y, et al. Microstructure and mechanics properties of interfaces between laser clad Inconel718 coating and substrate[J]. China Mechanical Engineering, 2019, 30(17): 2108-2113.
- [22] 黄春杰, 殷硕, 李文亚, 等. 冷喷涂技术及其系统的研究现状与展望[J]. 表面技术, 2021, 50(7): 1-23.
Huang C J, Yin S, Li W Y, et al. Cold spray technology and its system: research status and prospect[J]. Surface Technology, 2021, 50(7): 1-23.
- [23] 雒晓涛, 谢天, 李长久, 等. 冷喷涂金属的组织与性能调控[J]. 中国表面工程, 2020, 33(4): 68-81.
Luo X T, Xie T, Li C J, et al. Microstructure and properties tailoring of cold sprayed metals[J]. China Surface Engineering, 2020, 33(4): 68-81.
- [24] 吴洪键, 李文波, 邓春明, 等. 冷喷涂增材制造关键技术[J]. 中国表面工程, 2020, 33(4): 1-15.
Wu H J, Li W B, Deng C M, et al. Key techniques of cold spray additive manufacturing[J]. China Surface Engineering, 2020, 33(4): 1-15.
- [25] 石仲川, 王长亮, 汤智慧. 冷喷涂技术在轻合金再制造工程领域的研究现状[J]. 材料导报, 2014, 28(3): 97-99, 106.
Shi Z C, Wang C L, Tang Z H. Research progress on cold spray in light alloy remanufacturing engineering[J]. Materials Review, 2014, 28(3): 97-99, 106.
- [26] Widener C A, Carter M J, Ozdemir O C, et al. Application of high-pressure cold spray for an internal bore repair of a navy valve actuator[J]. Journal of Thermal Spray Technology, 2016, 25(1): 193-201.
- [27] Champagne V K. The repair of magnesium rotorcraft components by cold spray[J]. Journal of Failure Analysis and Prevention, 2008, 8(2): 164-175.
- [28] 张杰, 张群莉, 姚建华, 等. 激光熔覆 IN718 合金工艺优化及界面组织性能分析[J]. 中国激光, 2022, 49(16): 1602021.
Zhang J, Zhang Q L, Yao J H, et al. Process optimization and interface microstructure and properties analysis of laser clad IN718 alloy[J]. Chinese Journal of Lasers, 2022, 49(16): 1602021.
- [29] 潘浒, 赵剑峰, 刘云雷, 等. 激光熔覆修复镍基高温合金稀释率的可控性研究[J]. 中国激光, 2013, 40(4): 0403007.
Pan H, Zhao J F, Liu Y L, et al. Controllability research on dilution ratio of nickel-based superalloy by laser cladding repair[J]. Chinese Journal of Lasers, 2013, 40(4): 0403007.

Microstructures and Properties of Cold Spray-Laser Cladding Axle

Lv Peiyuan, Yu Min*, Luo Bin, Chen Qin, Chen Hui

Research Center of Sichuan Advanced Welding and Surface Engineering, School of Materials Science and Engineering, Southwest Jiaotong University, Chengdu 610031, Sichuan, China

Abstract

Objective Laser cladding has been used to repair damaged axles worldwide because of its low dilution rate, high metallurgical bonding strength, and controllable coating thickness. However, the heat input during the cladding process induces martensite transformation in the heat-affected zone (HAZ) of the steel substrate. The low plasticity and fracture toughness of martensite reduce the performance and service life of the axle. Therefore, reducing and eliminating the brittle and hard characteristics of martensite in HAZ have become a research focus. In this study, considering the deposition characteristics of no heat effect on the substrate of cold-spraying, the cold-spraying-laser cladding sequential coupling technology is preliminarily used to prepare a composite structure composed of a laser-clad Fe314 coating and a Ni30 cold-sprayed intermediate layer on the axle steel EA4T. This study aims to explore the influence of the cold-spraying interlayer on the microstructure and properties of laser-clad axle steel.

Methods Nd:YAG IPG-4000 laser and cold-spraying systems were used to prepare laser cladding and cold sprayed coatings,

respectively. First, a cold-sprayed Ni30 coating with a thickness of approximately 1 mm was prepared on the EA4T axle steel substrate, and then a Fe314 coating was laser-cladded on the cold-sprayed coating, the oxide film of which was removed by grinding. Simultaneously, a single laser-cladding Fe314 coating was prepared using the same process parameters for comparison. An optical microscope and a scanning electron microscope were used to observe the coating, HAZ, and micro-shear fracture morphologies. The distribution and content of the chemical elements in the samples were studied using an energy dispersive spectrometer equipped with a scanning electron microscope. The Vickers hardness of the coatings was tested using a digital microhardness tester with the loading of 200 g and the holding time of 15 s. A micro-shear test was performed on a mechanical testing machine.

Results and Discussions The cold-sprayed Ni30 coating is composed of extensively deformed Fe particles and unevenly distributed Ni particles. The pores and interfaces are clarified in the coating, and the coating is mechanically bonded to the substrate [Fig. 5(a)]. The average hardness of the cold-sprayed Ni30 coating is (229.89 ± 11.80) HV, and the hardness of the substrate is (234.63 ± 7.60) HV. The clad zone of the composite coating and that of single cladding coating are similar: owing to the effects of the temperature gradient G and solidification rate R , the grain morphology transfers from the plane crystal to the columnar crystal, and then to dendrites at the cladding layer bottom from the upward interface (Fig. 8), and the microstructures of both HAZs are martensite. The addition of the Ni30 layer has no effect on the morphologies of the cladding layer and HAZ, although it has a dilution effect on the laser cladding Fe314 layer in terms of the decrease in Fe content and increase in Ni content. This occurs at different alloy element contents at the interface after mutual diffusion. In addition, the absorption of laser heat by the cold-sprayed Ni30 reduces the area of the HAZ by 13.39% (Fig. 10). The laser heat causes the extensive plastic deformed Ni30 particle interface to melt, and the mechanical bonding of the cold-sprayed Ni30 coating with axle steel is changed to metallurgical bonding, increasing its shear strength from 35.9 MPa to 224.4 MPa. The average hardness of the clad zone of the composite sample is 275.1 HV, which is lower 56 HV than that of the single cladding, and the shear strength of the clad was slightly lower 25 MPa than that of the single cladding, and the cutting rate of the cross section increases by 53% (Fig. 13). Owing to the lower laser heat input into the HAZ of the composite cladding, the shear strength of the HAZ for the composite layer is lower (233.2 MPa) than that of the single cladding (Fig. 13). Finally, the fracture surfaces of the cladding and HAZ zone for the composite sample are covered with dimples and dense tear edges, suggesting a quasi-cleavage fracture (Fig. 14).

Conclusions The cold-sprayed Ni30 interlayer has no effect on the microstructure of the cladding or HAZ zones, although the area of HAZ decreases by 13.39%. The interface of the as-sprayed Ni30 intermediate layer is dissolved via laser heating.

The clad hardness of the composite sample is reduced to 275.1 HV, which is lower than the hardness value (331.8 HV) of the single cladding. The hardness of HAZ for the composite sample is reduced from 478.3 HV to 458.2 HV for the single cladding sample.

The shear strength of the cold-sprayed Ni30 interlayer and substrate for the composite sample is 224.4 MPa, which is lower than that (339.6 MPa) of the single cladding interface. The strength of the HAZ of the composite coating is lower by 233.2 MPa than that of the single cladding layer because of the lower heat input absorption of the cold-sprayed Ni30 interlayer.

Key words laser technique; laser cladding; cold spraying; heat-affected zone; structure and property